



HAL
open science

Germanium-rich nanoparticles in Cu-poor sphalerite: A new mechanism for Ge enrichment

Guotao Sun, Jia-Xi Zhou, Alexandre Cugerone, Mei-Fu Zhou, Lingli Zhou

► To cite this version:

Guotao Sun, Jia-Xi Zhou, Alexandre Cugerone, Mei-Fu Zhou, Lingli Zhou. Germanium-rich nanoparticles in Cu-poor sphalerite: A new mechanism for Ge enrichment. *Geological Society of America Bulletin*, 2023, 10.1130/B37014.1. . hal-04381658

HAL Id: hal-04381658

<https://hal.science/hal-04381658v1>

Submitted on 11 Jan 2024

HAL is a multi-disciplinary open access archive for the deposit and dissemination of scientific research documents, whether they are published or not. The documents may come from teaching and research institutions in France or abroad, or from public or private research centers.

L'archive ouverte pluridisciplinaire **HAL**, est destinée au dépôt et à la diffusion de documents scientifiques de niveau recherche, publiés ou non, émanant des établissements d'enseignement et de recherche français ou étrangers, des laboratoires publics ou privés.

1 *Guotao Sun et al.*

2 *Germanium-rich nanoparticles in sphalerite*

3 Guotao Sun[[ID](https://orcid.org/0000-0003-0698-6328)]<https://orcid.org/0000-0003-0698-6328>

4 †zhoujiaxi@ynu.edu.cn

5 *GSA Bulletin*; Month/Month 2024; v. 136; no. X/X; p. 000–000;

6 <https://doi.org/10.1130/B37014.1>; 16 figures; 2 tables; 1 supplemental file.

7 ¹Supplemental Material. LA-ICP-MS trace-element data of sphalerite from the Banbianjie
8 deposit. Please visit <https://doi.org/10.1130/GSAB.S.XXXX> to access the supplemental material,
9 and contact editing@geosociety.org with any questions.

10 SCIENCE EDITOR: BRAD SINGER

11 ASSOCIATE EDITOR: SANTIAGO TASSARA

12 MANUSCRIPT RECEIVED 5 MARCH 2023

13 REVISED MANUSCRIPT RECEIVED 14 SEPTEMBER 2023

14 MANUSCRIPT ACCEPTED ___ MONTH 2023

15 Printed in the USA

16 Germanium-rich nanoparticles in Cu-poor sphalerite: A new 17 mechanism for Ge enrichment

18 **Guotao Sun^{1,2}, Jia-xi Zhou^{1,3,†}, Alexandre Cugerone⁴, Mei-fu Zhou⁵, and Lingli Zhou⁶**

19 ¹*School of Earth Sciences, Yunnan University, Kunming 650500, China*

20 ²*College of Resources and Environmental Engineering, Guizhou University, Guiyang 550012,*
21 *China*

22 ³*Key Laboratory of Critical Minerals Metallogeny, University of Yunnan Province, Kunming*
23 *650500, China*

24 ⁴*Department of Earth Sciences, University of Geneva, Geneva 1205, Switzerland*

25 ⁵*State Key Laboratory of Ore Deposit Geochemistry, Institute of Geochemistry, Chinese*
26 *Academy of Sciences, Guiyang 550081, China*

27 ⁶*Faculty of Science, Vrije University Amsterdam, Amsterdam 1105, Netherlands*

28 **ABSTRACT**

29 Germanium (Ge) is a critical raw material used in high-technology industry (i.e., optical
30 industry) **applications**, and it is predominantly concentrated in coals and Zn-rich deposits.
31 Previous studies on Zn-rich deposits have documented a correlation between Ge enrichment and
32 the Cu, Ag, and/or Pb-Mn contents in the sphalerite crystal lattice. In this study, we observed Ge-
33 rich nanoparticles hosted in Cu-poor sphalerite from the Banbianjie Zn-Ge deposit (>800 t
34 **graded at** ~100 ppm Ge), located in southwest China. Laser-ablation–inductively coupled
35 **plasma**–mass spectroscopy (LA-ICP-MS) analyses revealed that sphalerite contains very
36 heterogeneous Ge contents (172–1553 ppm). Germanium contents showed positive correlations
37 with Fe, Mn, and Pb contents and negative correlations with Cd contents. Higher Ge contents
38 were detected in the darker zones, whereas the lighter zones showed systematically low Ge
39 contents and were enriched in Cd. Using transmission electron microscopy (TEM), Zn-Ge-Pb-S

40 nanoparticles were identified in the darker zones of sphalerite. These nanoparticles exhibited
 41 Ge/Pb ratios (0.48–1.96) very similar to those measured in sphalerite (0.36–2.04), suggesting
 42 that Ge could be essentially hosted within the nanoparticles. We propose that the amounts of Zn-
 43 Ge-Pb-S nanoparticles are related to a self-organization model induced by rapid crystal growth.
 44 This self-organization processes may control the fluctuations of element concentrations in the
 45 boundary layer. This study highlights the importance of studying the nanoscale expression of
 46 critical elements to understand their incorporation mechanisms into natural materials.

47 INTRODUCTION

48 Critical raw materials such as germanium (Ge) are key **factors** in the high-tech industry
 49 with various applications in the so-called “green” technologies (Gulley et al., 2018; Wang, 2019;
 50 Zhai et al., 2019; Cugerone et al., 2020; Zhou et al., 2021 [2021a or 2021b?]); Kelley et al.,
 51 2021), such as infrared goggles for military use (Gulley et al., 2018), high-performance fiber-
 52 optic cables for internet, and semiconductor materials for multijunction solar cells (Frenzel et al.,
 53 2014). Germanium is mainly extracted as a by-product of coal and **base** metal (Pb-Zn) deposits,
 54 mostly from sphalerite (Frenzel et al., 2014, 2017; Paradis, 2015; Lawley et al., 2022 [N₁
 55 **reference list.**]); Torr o et al., 2023). A significant increase in the production of Ge has occurred
 56 in the past 20 yr from 45 to 140 t/yr (U.S. Geological Survey, 1996, 2022). To deal with this
 57 increasing demand, the general distribution and mechanism(s) of concentrations of Ge in Zn ore
 58 need to be better understood to constrain the Ge resource potential of given base metal deposits
 59 in an economically and environmentally sustainable manner (Liu et al., 2023).

60 Carbonate-hosted base metal (Pb-Zn) deposits associated with low-temperature fluids
 61 (<150  C) are generally richer in Ge (Fig. 1). For example, the world-class Huize carbonate-
 62 hosted deposit contains 525 t graded at 93 ppm Ge (Fig. 1; Tao et al., 2019). Sphalerite is the
 63 main host mineral for Ge in carbonate-hosted deposits. Previous studies have revealed that Ge is
 64 incorporated into the sphalerite crystal lattice through substitution of Zn²⁺ coupled with
 65 monovalent cations such as Cu⁺ and Ag⁺ (Johan, 1988; Cook et al., 2009; Belissont et al., 2014,
 66 2016; Bonnet et al., 2016; Bauer et al., 2019; Torr o et al., 2023) and more complex substitutions
 67 involving divalent cations such as Pb²⁺ and/or Mn²⁺ (Luo et al., 2022). It is noteworthy that the
 68 metamorphism of Ge-rich sphalerite may induce the redistribution of Ge and the formation of
 69 micro- to nanoscale Ge minerals (e.g., brunogeierite and briartite; H oll et al., 2007; Cugerone et
 70 al., 2018, 2020; Fougrouse et al., 2023).

71 Newly reported Ge resources in the Huangsi region (SW China) reach >1200 t, mostly
 72 located in the Banbianjie (>800 t) and Zhulingou (>400 t) deposits (Fig. 1; Zhou et al.,
 73 2021 [2021a or 2021b?]); Luo et al., 2022). More specifically, the Banbianjie deposit contains
 74 resources of 0.8 Mt graded at 1.78%–9.5% Zn and mean grades of ~100 ppm Ge (An et al.,
 75 2022). Previous studies constrained the origin and geological conditions of the Ge enrichment in
 76 sphalerite in the Banbianjie and Huangsi region (An et al., 2022; Luo et al., 2022) without
 77 reporting the micro- to nanoscale distribution of Ge in sphalerite.

78 Here, we focused on the spatial distribution of Ge in sphalerite. Focused ion beam-
 79 scanning electron microscopy (FIB-SEM) and transmission electron microscopy (TEM) analyses

80 were applied to **characterize** the nanoscale distribution of Ge in sphalerite. We also propose a
81 schematic model for the enrichment of Ge in the Banbianjie deposit.

82 REGIONAL GEOLOGY

83 The southeast margin of the Yangtze block (Fig. 2A) **contains** late Proterozoic
84 metamorphic and metasedimentary rocks and Cambrian to Permian–Triassic sedimentary rocks
85 (Fig. 2B). The Proterozoic metamorphic rocks belong to the Banxi Group and include
86 **graywacke**, slate, and schist. The Banxi Group has undergone low-grade greenschist-facies
87 metamorphism (Wang et al., 2010). U-Pb zircon ages of tuff and tuffaceous rocks in the Banxi
88 Group constrain its deposition between ca. 820 **Ma** and 715 Ma (Lan et al., 2014, 2015; Li et al.,
89 2019; Xian et al., 2020). The Cambrian to Silurian sedimentary succession consists of a shale-
90 carbonate-siliciclastic transition, indicating either a regression of sea level or the uplift of the
91 southeastern Yangtze block (Yao and Li, 2016). The Devonian to Triassic succession comprises
92 sandstone, wackestone, dolostone, limestone, and shale and records at least three cycles of
93 transgression-regression (GBGMR, 1987).

94 The structural framework of the Huangsi region is dominant by N-S, E-W, and **NE-NW-**
95 trending **[[Please verify last direction here: Should be NE-SW? or SE-NE?]]** structures (Fig.
96 2B). The N-S–striking structures dominantly comprise box anticlines (e.g., the Huangsi and
97 Wangsi anticlines) and chevron synclines (e.g., the Duyun syncline; Fig. 2B). These structures
98 are frequently cut by N-S–striking thrust faults (Fig. 2B). The Wangsi anticline is cut by N-S–
99 and NE-SW–striking normal faults, whereas the Huangsi anticline is cut by E-W–striking normal
100 faults (e.g., Huangsi fault; Fig. 2B).

101 BANBIANJIE DEPOSIT, SOUTHWEST CHINA

102 Deposit Geology

103 The Banbianjie district is mainly composed of Silurian to Middle Devonian clastic rocks,
104 Upper Devonian dolostone, Carboniferous carbonate, and Permian clastic rocks (Chen et al.,
105 2006). The ore bodies are hosted in the Devonian Gaopochang Formation (Fig. 3A), which
106 shows a variable thickness in the range between 380 **m** and 1074 m. The biostratigraphy suggests
107 that the Gaopochang Formation was deposited between ca. 385 **Ma** and 360 Ma (Chen et al.,
108 2006). The lower part of the Gaopochang Formation consists of dark-gray, fine-grained
109 dolostone and argillaceous dolostone (Figs. 3B–3C). The middle part is characterized by dark-
110 gray, thick-bedded, bioclastic dolostone interbedded with restricted black, grayish-yellow, and
111 grayish-green mudstone (Figs. 3B–3C). A characteristic feature of the dolostone in the middle
112 part is the abundance of centimeter-scale geodes composed of dolomite (Figs. 4A–4B). The
113 upper part of the Gaopochang Formation is dominantly composed of thick, light-gray or gray,
114 fine-grained dolostone, with a minor proportion of argillaceous dolostone. The Zn-Ge
115 mineralization occurs mainly in the middle part of the Gaopochang Formation (Figs. 3B–3C).

116 In the mining area, the main structures are the E-W–striking Banbianjie anticline and the
117 Huangsi fault zone. The Huangsi fault zone crosscuts the south limb of the Banbianjie anticline
118 (Fig. 3A; Chen et al., 2006) and comprises a set of E-W–striking faults with a general dip of
119 40°–70° to the south. Chen et al. (2006) suggested that **activity on** the fault zone **was**
120 synsedimentary and controlled the lithofacies of the Gaopochang Formation. However, the fact

121 that the Carboniferous–Triassic rocks are crosscut by the Huangsi fault would indicate that the
122 Huangsi fault was reactivated after the Carboniferous.

123 **Ore Bodies**

124 The Zn-Ge mineralization, which is hosted exclusively in the middle part of the
125 Gaopochang dolostone, comprises six stratabound and lenticular ore bodies. Mineralization is
126 hosted in bedded dark-gray dolostone with a fine-crystalline texture (Figs. 4A–4B). The No. 2
127 ore body, the largest one in Banbianjie, has a thickness ranging from 1.13 m to 11.8 m, and it
128 contains ore with Zn grades between 1.78% and 9.5% and Ge grades of ~100 g/t. The ore bodies
129 are composed of multiple Zn-rich veins that are parallel to or crosscut the bedding of the dark-
130 gray dolostone (Figs. 4A–4B). These veins vary in thickness, from 1 cm to 50 cm, and in texture,
131 locally showing brecciated texture (Fig. 4C). In the breccia, the clasts are rounded and cemented
132 by sulfide minerals. Sulfides in the veins show macroscopic oscillatory zoning (Fig. 4D).

133 **SAMPLING AND ANALYTICAL METHODS**

134 Samples from the Banbianjie deposit were collected from underground galleries and drill
135 cores. Forty-five thin sections were studied with optical microscopy and scanning electron
136 microscopy (SEM). Among them, sphalerite in samples BBJ-1, BBJ-5, and ZK1008 was
137 analyzed by laser-ablation–inductively coupled plasma–mass spectroscopy (LA-ICP-MS) for
138 trace elements. Colloform sphalerite in samples BBJ-1 and ZK1008 was selected for elemental
139 mapping by LA-ICP-MS.

140 **SEM Analysis**

141 SEM analyses were carried out on a JSM7800F SEM at the State Key Laboratory of Ore
142 Deposit Geochemistry, Institute of Geochemistry, Chinese Academy of Sciences (IGCAS),
143 Guiyang, China. The backscattered electron (BSE) images were collected with a voltage of 20
144 kV.

145 **FIB/SEM and TEM Analyses**

146 The FIB combined with SEM imaging was conducted on an FEI Scios dual-beam
147 FIB/SEM at the IGCAS. The FIB/SEM system was used for the preparation of TEM foils. A
148 sphalerite area with ~400 ppm of Ge was selected for the FIB milling. The TEM foil had a
149 dimension of $10 \times 10 \times 0.06 \mu\text{m}$.

150 The TEM analysis was conducted on an FEI Tecnai G2 F20 TEM equipped with a Gatan
151 imaging filter, an energy-dispersive X-ray analyzer with an ultrathin window, and a Fischione
152 high-angle annular dark-field (HAADF) detector at the IGCAS. The HAADF images were taken
153 by a camera with a length of 75 mm, which can avoid the influence of Bragg scattered electrons.
154 Energy-dispersive X-ray spectroscopy (EDS) was conducted using the TEM in scanning
155 transmission mode. The acquisition time was 120–240 s. The detector conditions included an
156 energy resolution of 134 eV, a reference energy of 5.9 keV, a detector distance of 11.8 mm, and
157 a detector angle of 14.6° . The microscope conditions included an acceleration voltage of 200 kV
158 and a beam current of 1 nA. The spot sizes were 5–10 nm to avoid the influence of the host. The
159 spectral lines analyzed for each element were S ($K\alpha$), Fe ($K\alpha$), Zn ($K\alpha$), Ge ($K\alpha$), and Pb ($L\alpha$).
160 Further details of the analytical procedure can be found in Liang et al. (2021).

161 **LA-ICP-MS Trace-Element Analyses**

162 Trace-element contents of sphalerite were determined by LA-ICP-MS at the Guangzhou
 163 Tuoyan Analytical Technology Co., Ltd., Guangzhou, China. The samples were analyzed using
 164 an iCAP RQ ICP-MS instrument equipped with a NWR ablation system ($\lambda = 193$ nm). The
 165 operating conditions were a frequency of 8 Hz and a laser spot size of 30 μm . NIST610, GSE-
 166 2G, and MASS-1 were used as external standards for calibration, and ^{66}Zn (Zn = 650,000 ppm)
 167 was used as the internal standard. Each analysis consisted of 50 s of background measurement
 168 and 40 s of sample ablation (signal measurement). The time-integrated LA-ICP-MS signals were
 169 processed using Iolite v3.25 (Paton et al., 2011).

170 For LA-ICP-MS mapping, the operating conditions were a fluence of 1.5 J/cm², a
 171 repetition rate of 40 Hz, and a washout time of 20 s. Two laser-spot sizes were used depending
 172 on the thickness of the zoning bands (~~15- μm spot size measurements are shown in Fig. 9~~ **[GSA**
 173 **style requires all figures to be cited in numerical order. Please move the first citation to**
 174 **Figure 9 between the first citations to Figure 8 and Figure 10 or renumber figures.]]**; ~~20- μm~~
 175 ~~spot size measurements are shown in Fig. 10~~ **[Per GSA style, please move the first citation to**
 176 **Figure 10 between the first citations to Figure 9 and Figure 11 or renumber figures.]]). To**
 177 produce the elemental maps, adjacent lines were ablated successively. A square-shaped laser
 178 aperture was progressively translated by a continuous movement of the stage under the fixed
 179 ablation site to generate an evenly ablated line (see Zhou et al., 2017). NIST 610, GSE-2G, and
 180 MASS-1 were analyzed as external standards (Wilson et al., 2002). The external standards were
 181 ablated three times, before, in between, and after the analysis mapping of each area. Each
 182 analytical procedure involved the analysis of 16 elements: ^{34}S , ^{55}Mn , ^{57}Fe , ^{59}Co , ^{60}Ni , ^{65}Cu , ^{66}Zn ,
 183 ^{71}Ga , ^{74}Ge , ^{75}As , ^{77}Se , ^{107}Ag , ^{111}Cd , ^{115}In , ^{118}Sn , and ^{208}Pb . The elemental maps were generated
 184 using Iolite v3.25, which runs with Igopro (Paton et al., 2011). Further details on the analytical
 185 procedure can be found in Zhou et al. (2017).

186 MATLAB-based package XMapTools was applied to quantify and extract the measured
 187 contents from the elemental mapping data. The quantified data for each element (ppm) were first
 188 exported using Iolite. XMapTools can visualize and explore these data via line model sampling
 189 functions, via pixel identification maps, or via histogram, binary, and/or **ternary** diagrams (see
 190 Lanari et al., 2014; Raimondo et al., 2017; Sun et al., 2021).

191 RESULTS

192 Texture and Mineralogy

193 Two types of ore were recognized in the Banbianjie deposit (Figs. 4A–4G). Type 1 ore
 194 consisted mostly of centimeter-scale veins (Figs. 4A, 4B, and 4D) with red- to brown colloform
 195 sphalerite (Sp1b; Figs. 4D and 5A–5E), pyrite (Py1b), and acicular marcasite with minor
 196 dolomite, barite, and calcite. The thicknesses of individual sphalerite and pyrite layers varied
 197 from 1 **mm** to 5 mm (Figs. 5A and 5E). Under the microscope with transmitted light, the
 198 colloform Sp1b showed oscillatory color zoning with black to light-yellow color zones. The
 199 black-to-brown-colored Sp1b crystals were acicular and oriented perpendicular to the color
 200 zoning boundaries (Figs. 5B and 5F). However, light-yellow-colored Sp1b generally consisted
 201 of euhedral sphalerite crystals (Figs. 5B and 5F). Acicular marcasite crystals were intergrown
 202 with euhedral pyrite aggregates (Fig. 5C). Locally, some sulfide-rich areas were more fractured,

203 and deformed textures were observed with characteristic coarse sphalerite surrounded by fine
204 sphalerite crystals (<100 μm ; Fig. 5D). Type 1 ore was locally composed of subhedral sphalerite
205 and pyrite crystals disseminated in the dolostone host (Sp1a and Py1a; Fig. 5A).

206 Type 2 ore occurred as veinlets filling fractures or as globular aggregates generally
207 thinner than type 1 ore (Figs. 4E–4G); it was composed of colloform sphalerite (Sp2), with
208 minor pyrite (Py2), marcasite (Mas2), and galena in a gangue of dolomite and calcite (Figs. 6A
209 and 6E). Angular sphalerite clasts of type 1 ore were cemented by dolomite and crosscut by the
210 type 2 ore (Figs. 6A–6D). Sp2 comprised oscillatory zones of yellow to brown colors (Figs. 4E–
211 4G and 6C). In general, oscillatory color zoning textures in acicular Sp2 were more complex and
212 intense compared to Sp1 (Figs. 6B, 6C, and 7).

213 **Chemical Composition of Sphalerite**

214 ***Spot Analyses***

215 LA-ICP-MS results of sphalerite included three analyses of Sp1a, 28 analyses of Sp1b,
216 and 23 analyses of Sp2 (Table 1; Supplemental Material¹).

217 Sp1a contained relatively high Fe, Cd, Ge, and Pb contents with 7798–9773 ppm, 471–
218 484 ppm, 578–683 ppm, and 985–1286 ppm, respectively (Supplemental Material). Detectable
219 Mn and Tl contents are also observed in Sp1a (34–41 ppm and 28–36 ppm, respectively). The
220 contents of Cu, Ga, Ag, and Sn were systematically below 10 ppm (1.67–1.89 ppm, 1.66–3.43
221 ppm, 1.89–2.35 ppm, and 2.04–7.86 ppm, respectively). Germanium contents were higher in
222 Sp1b than in Sp1a and ranged between 236 ppm and 1553 ppm, with a mean value of 720 ppm.
223 Contents of Mn, Fe, Ag, Cd, and Tl in Sp1b were similar to those of Sp1a (Fig. 8), whereas the
224 Ga, Ge, In, and Pb contents were higher than those of Sp1a (Fig. 8). Compared with Sp1a and
225 Sp1b, Sp2 exhibited similar contents of Mn (21.0–79.1 ppm), Fe (7716–19,466 ppm), Cu (0.41–
226 19.2 ppm), Tl (5.41–56.1 ppm), and Pb (27.0–849 ppm), but higher contents of Ga (1.95–21.2
227 ppm), As (0.17–5.30), and Cd (232–2862 ppm), and lower contents of Ag (0.28–0.52 ppm) and
228 Hg (1.46–3.38 ppm; Fig. 8). In Sp2, Ge contents ranged 306–1150 ppm, with a mean value of
229 706 ppm, which is similar to Sp1b.

230 **Spatial Distribution of Elements**

231 The spatial distributions of Fe, Mn, Ga, Ge, Ag, Cd, and Pb are illustrated for Sp1b and
232 Sp2 in Figures 9, 10, and 11. The compositional maps revealed a very heterogeneous zoning in
233 Sp1b and Sp2, frequently correlating with microscopic color zoning (Figs. 9 and 10). In Sp1b,
234 the darker color zones were richer in Fe, Ge, Mn, In, Ag, and Pb and generally depleted in Cd
235 and Ga; in contrast, the lighter color zones were frequently richer in Cd and Ga and depleted in
236 Fe, Ge, Mn, In, Ag, and Pb compared to the dark color zones (Fig. 9). Nevertheless, local areas
237 in the light color zones were also depleted in Cd and Ga. Compositional analyses performed
238 along a transect (Figs. 11A–11D) showed that Ge contents were mainly correlated to Fe, Mn, and
239 Pb and anticorrelated to Cd and Ga.

240 In Sp2, a more complex zoning was identified. The darker zones were enriched in Fe,
241 Mn, Ga, Ge, In, and Pb, whereas the lighter zones were frequently enriched in Cd. The main
242 difference in the trace-element distributions between Sp1b and Sp2 was that Ga was positively
243 correlated with Cd in Sp1b (Figs. 11C–11D) but was anticorrelated with Cd in Sp2 (Fig. 11E).

244 More precisely, two types of zoning were observed in Sp2. In the bottom part, the zones with
 245 higher Ge contents had thicknesses from 500 μm to 2000 μm , i.e., thicker than the zones (300–
 246 600 μm) with lower Ge contents. In the upper part, the Ge-richer and Ge-poorer zones had
 247 similar thicknesses from 150 μm to 200 μm .

248 **Compositions of Nanoscale Particles**

249 At the nanoscale, the HAADF-TEM images performed on Sp1b revealed the occurrence
 250 of anhedral nanoparticles with sizes from 10 to 70 nm (Figs. 12A–12F). These nanoparticles
 251 were analyzed with EDS and consisted mainly of S, Zn, Ge, and Pb (Table 2). The contents of S,
 252 Zn, Ge, and Pb had ranges of 24.3–33.2 wt%, 32.3–58.9 wt%, 3.34–11.2 wt%, and 12.4–28.6
 253 wt%, respectively.

254 **DISCUSSION**

255 **Germanium Incorporation in Sphalerite**

256 In Cu-Ag-depleted Sp1 and Sp2 (Cu < 19.2 ppm, Ag < 5.6 ppm), Ge contents were
 257 positively correlated with Fe, Mn, and Pb (Figs. 13A, 13C, and 13E). This differs from the
 258 previously documented positive correlation between Ge and Cu or Ag (Ye et al., 2011; Belissont
 259 et al., 2014; Bauer et al., 2019; Torró et al., 2023). At the microscale, the weak correlation ($R^2 =$
 260 0.14) between Ge and Fe (Fig. 13A) in our analyses may exclude a $\text{Ge}^{4+} + \text{Fe}^{2+} + \square \leftrightarrow 3\text{Zn}^{2+}$
 261 [\[\[Please verify symbol in expression here.\]\]](#) coupled substitution (Cook et al., 2009; Luo et al.,
 262 2022). However, Ge was also positively correlated ($R^2 = 0.75$ and 0.56 , respectively) with Mn
 263 and Pb (Figs. 13C and 13E; 1:10 ratio for Mn), which may imply complex substitution
 264 mechanisms if Ge was hosted in the sphalerite lattice. Our study was therefore conducted with a
 265 nanoscale survey to determine the precise Ge host and incorporation mechanisms.

266 TEM analysis revealed the occurrence of Zn-, Ge-, Pb-, and S-rich nanoparticles within
 267 Sp1b. Unfortunately, Ge and Pb contents in sphalerite were not measured due to the high lower
 268 limits of detection of EDS (1–2 wt% Ge or Pb). An indirect method, comparing Ge/Pb ratios
 269 measured with LA-ICP-MS and EDS, was used to determine if the nanoparticles were the
 270 dominant hosts of Ge. The Ge/Pb ratios of sphalerite can reflect the amounts of nanoparticles. In
 271 Sp1a, Sp1b, and Sp2, the Ge and Pb contents measured with LA-ICP-MS and contents in
 272 nanoparticles measured with TEM-EDS were positively correlated ($R^2 = 0.85$) with a ratio of
 273 Ge/Pb ~ 1 (Fig. 14A). Furthermore, the LA-ICP-MS spot analyses in Sp1a, Sp1b, and Sp2 had
 274 Ge/Pb ratios similar to the TEM-EDS analyses on the nanoparticles (between 0.48 and 1.96, with
 275 a mean of 1.09; Fig. 14B). As the Pb is hardly incorporated into sphalerite (Cook et al., 2009;
 276 George et al., 2016), this result suggests that Ge and Pb mainly occur as Zn-Ge-Pb-S
 277 nanoparticles.

278 The extracted chemical composition from the LA-ICP-MS mapping of sphalerite,
 279 comprising >80,000 measurements, showed that Ge and Pb were positively correlated in Sp1b
 280 and Sp2 (Figs. 15A and 15D). The quantified compositional profiles (Figs. 15C and 15F) showed
 281 that Ge and Pb had similar distribution patterns in both Sp1b and Sp2. The calculated Ge/Pb
 282 ratios of Sp1b and Sp2 mainly ranged from 0.30 to 2.0 and from 0.36 to 2.0, respectively, which
 283 are consistent with the ratios in the Zn-Ge-Pb-S nanoparticles measured with TEM-EDS. These

284 results likely suggest that the Zn-Ge-Pb-S nanoparticles are the predominant phase hosting Ge in
285 the Banbianjie deposit.

286 **Formation of Ge Oscillatory Zoning in Sphalerite**

287 Previous studies have suggested that oscillatory chemical zoning observed in minerals,
288 including sphalerite and pyrite, may reflect self-organized nonequilibrium processes during
289 crystal growth (Fowler and L'Heureux, 1996; Di Benedetto et al., 2005; Wu et al., 2019;
290 Fougereuse et al., 2023). In the Banbianjie deposit, the colloform texture may suggest a rapid
291 growth rate (Abraitis et al., 2004; Franchini et al., 2015), which may have been faster than the
292 diffusion rate and allowed self-organization processes (Fowler and L'Heureux, 1996; Phelps et
293 al., 2020). The Fe (Mn) and Cd patterns are antithetic in sphalerite from Banbianjie (Figs. 9, 10,
294 11, and 15), suggesting that Fe (Mn) may compete with Cd to replace Zn. Both Fe^{2+} (0.63 Å) and
295 Mn^{2+} (0.66 Å) have ionic radii similar to Zn^{2+} (0.60 Å), whereas Cd^{2+} (0.78 Å) is slightly larger
296 than Zn^{2+} . This difference in ionic radius could explain the initial zoning in sphalerite, which is
297 usually Fe- and Mn-rich and Cd-poor (Figs. 9, 10, and 16A). When the fluid becomes depleted in
298 Fe (Mn), Cd starts to be incorporated into sphalerite, following a typical feedback reaction
299 pathway (Figs. 16A and 16B). The feedback processes represent the self-organization that
300 controls the fluid composition at the boundary layer and, consequently, the formation of
301 oscillatory zoning textures (Di Benedetto et al., 2005). Similarly, the Ga^{3+} (0.47 Å) and In^{3+}
302 (0.62 Å) ions may also compete with each other to combine with monovalent cations (e.g., Cu^+
303 and Ag^+) and to substitute for Zn^{2+} (0.60 Å). In Sp1b, Ga and In are anticorrelated (Fig. 9), and
304 the initial zoning of Sp1b is In-rich (Fig. 9), which is consistent with the fact that the size of In^{3+}
305 is very similar to that of Zn^{2+} , compared to the ionic radius of Ga^{3+} . In Sp2 (Fig. 10), In contents
306 were very low (0.01–0.87 ppm), probably due to the primary fluid composition preventing
307 competition and self-organization processes between Ga and In.

308 The Ge oscillatory zoning showed a correlation with Fe and Mn contents, suggesting that
309 the Zn-Ge-Pb-S nanoparticles may also be a consequence of self-organization. In our model,
310 self-organization controlled the element concentrations in the boundary layer. Abundant Zn^{2+} ,
311 Fe^{2+} , Mn^{2+} , Ge^{4+} , and Pb^{2+} in the boundary layer may have reacted with HS^- , triggering the
312 precipitation of Zn-Ge-Pb-S nanoparticles and acicular sphalerite. Because the growth rate was
313 faster than the diffusion rate, cations such as Zn, Ge, Fe, Mn, and Pb were likely depleted at the
314 boundary layer (Phelps et al., 2020), which resulted in a decrease of the abundance of Zn-Ge-Pb-
315 S nanoparticles and slower growth rates of euhedral sphalerite (Figs. 16A and 16B). This process
316 was cyclical, and before the next precipitation event, the concentrations of Zn, Ge, Fe, Mn, and
317 Pb in the boundary layer would have increased to form a new acicular sphalerite layer rich in
318 nanoparticles (Figs. 16A and 16B).

319 In classical carbonate-hosted Pb-Zn deposits, Ge is commonly described as occurring in
320 the sphalerite crystal lattice coupled with other metal ions (e.g., Cu^+ , Ag^+ , Mn^{2+} , Pb^{2+} ; Belissant
321 et al., 2016; Luo et al., 2022; Liu et al., 2023; Torró et al., 2023). In our study, we showed that
322 Ge mostly occurs in Zn-Ge-Pb-S nanoparticles within sphalerite. A sphalerite poor in Cu and fast
323 crystal growth may be prerequisites for the formation of nanoparticles. Other particular physico-
324 chemical conditions (e.g., pH, redox, fluid compositions) may finally result in the precipitation

325 of the nanoparticles. Additional experiments are needed to better constrain their mode of
 326 occurrence and distribution, considering that they represent low-temperature hydrothermal
 327 systems in which Ge is highly enriched.

328 CONCLUSIONS

329 Sphalerite from the Banbianjie deposit showed high contents of Ge (up to 1553 ppm).
 330 The distribution of Ge in colloform sphalerite showed oscillatory zoning with higher Ge
 331 enrichment in darker sphalerite, positive correlations between Ge and Fe, Pb, and Mn, and a
 332 negative correlation with Cd. We documented the occurrence of Zn-Ge-Pb-S nanoparticles.
 333 Based on TEM and LA-ICP-MS analyses, these nanoparticles may be the dominant host for Ge
 334 due to the similar Ge/Pb ratios measured in both the Zn-Ge-Pb-S nanoparticles and the host
 335 sphalerite. The oscillatory chemical zoning (including Ge) in sphalerite may be related to self-
 336 organization processes, which resulted in the fluctuations of various trace-element concentrations
 337 in the boundary layer. The element concentrations in the boundary layer may further have
 338 influenced the growth rate and texture of the sphalerite. This study showed the **ability** of
 339 nanoscale studies to unravel the incorporation mechanisms of critical elements in sphalerite, a
 340 key component for critical raw material exploration and ore processing.

341 ACKNOWLEDGMENTS

342 We acknowledge funding of this research by the National Natural Science Foundation,
 343 China (~~42263010, 42172082~~, U1812402, 92162218, 42372103), the Research Startup Project of
 344 Yunnan University, China (YJRC4201804), Guizhou Provincial Science and Technology
 345 Projects (Qiankehejichu-ZK[2023]Yiban064), and Major Collaborative Innovation Projects for
 346 Prospecting Breakthrough Strategic Action of Guizhou Province, China ([2022] ZD004). Thanks
 347 **go** to the 104 Geological Brigade of Guizhou Bureau of Geology and Mineral Resources for field
 348 support. We would like to thank the FIB-SEM Laboratory and TEM Laboratory of IGCAS for
 349 their analytical work. We also thank Lisard Torró and Denis Fougereuse for their constructive
 350 reviews.

351 REFERENCES CITED

- 352 Abraitis, P.K., Patrick, R.A.D., and Vaughan, D.J., 2004, Variations in the compositional,
 353 textural and electrical properties of natural pyrite: A review: *International Journal of Mineral*
 354 *Processing*, v. 74, no. 1–4, p. 41–59, <https://doi.org/10.1016/j.minpro.2003.09.002>.
 355 An, Y.-L., Luo, K., Zhou, J.-X., Nguyen, A., Lu, M.-D., Meng, Q.-T., and An, Q., 2022, Origin
 356 of the Devonian carbonate-hosted Banbianjie Ge-Zn deposit, Guizhou Province, South
 357 China: Geological, mineralogical and geochemical constraints: *Ore Geology Reviews*,
 358 v. 142, <https://doi.org/10.1016/j.oregeorev.2022.104696>.
 359 **[[Not cited in text.]]** Barker, S.L.L., and Cox, S.F., 2011, Oscillatory zoning and trace element
 360 incorporation in hydrothermal minerals: Insights from calcite growth experiments:
 361 *Geofluids*, v. 11, no. 1, p. 48–56, <https://doi.org/10.1111/j.1468-8123.2010.00305.x>.
 362 Bauer, M.E., Burisch, M., Ostendorf, J., Krause, J., Frenzel, M., Seifert, T., and Gutzmer, J.,
 363 2019, Trace element geochemistry of sphalerite in contrasting hydrothermal fluid systems of
 364 the Freiberg district, Germany: Insights from LA-ICP-MS analysis, near-infrared light

- 365 microthermometry of sphalerite-hosted fluid inclusions, and sulfur isotope geochemistry:
366 Mineralium Deposita, v. 54, p. 237–262, <https://doi.org/10.1007/s00126-018-0850-0>.
- 367 Belissant, R., Boiron, M.-C., Luais, B., and Cathelineau, M., 2014, LA-ICP-MS analyses of
368 minor and trace elements and bulk Ge isotopes in zoned Ge-rich sphalerites from the
369 Noailhac–Saint-Salvy deposit (France): Insights into incorporation mechanisms and ore
370 deposition processes: *Geochimica et Cosmochimica Acta*, v. 126, p. 518–540,
371 <https://doi.org/10.1016/j.gca.2013.10.052>.
- 372 Belissant, R., Muñoz, M., Boiron, M.-C., Luais, B., and Mathon, O., 2016, Distribution and
373 oxidation state of Ge, Cu and Fe in sphalerite by μ -XRF and K-edge μ -XANES: Insights
374 into Ge incorporation, partitioning and isotopic fractionation: *Geochimica et Cosmochimica*
375 *Acta*, v. 177, p. 298–314, <https://doi.org/10.1016/j.gca.2016.01.001>.
- 376 Bonnet, J., Mosser-Ruck, R., Caumon, M.-C., Rouer, O., Andre-Mayer, A.-S., Cauzid, J., and
377 Peiffert, C., 2016, Trace element distribution (Cu, Ga, Ge, Cd, and Fe) in sphalerite from the
378 Tennessee MVT deposits, USA, by combined EMPA, LA-ICP-MS, Raman spectroscopy,
379 and crystallography: *Canadian Mineralogist*, v. 54, p. 1261–1284,
380 <https://doi.org/10.3749/canmin.1500104>.
- 381 Chen, G.Y., An, Q., and Wang, M., 2006, Geological characteristics and genesis of the
382 Banbianjie type lead-zinc deposits in southern Guizhou Province: *Acta Geoscientica Sinica*,
383 v. 27, p. 570–576 [in Chinese with English abstract].
- 384 Cook, N.J., Ciobanu, C.L., Pring, A., Skinner, W., Shimizu, M., Danyushevsky, L., Saini-
385 Eidukat, B., and Melcher, F., 2009, Trace and minor elements in sphalerite: A LA-ICPMS
386 study: *Geochimica et Cosmochimica Acta*, v. 73, p. 4761–4791,
387 <https://doi.org/10.1016/j.gca.2009.05.045>.
- 388 **[[Not cited in text.]]** Corbella, M., Ayora, C., and Cardellach, E., 2004, Hydrothermal mixing,
389 carbonate dissolution and sulfide precipitation in Mississippi Valley–type deposits:
390 *Mineralium Deposita*, v. 39, p. 344–357, <https://doi.org/10.1007/s00126-004-0412-5>.
- 391 Cugerone, A., Cenki-Tok, B., Chauvet, A., Le Goff, E., Bailly, L., Alard, O., and Allard, M.,
392 2018, Relationships between the occurrence of accessory Ge-minerals and sphalerite in
393 Variscan Pb-Zn deposits of the Bossost anticlinorium, French Pyrenean Axial zone:
394 Chemistry, microstructures and ore-deposit setting: *Ore Geology Reviews*, v. 95, p. 1–19,
395 <https://doi.org/10.1016/j.oregeorev.2018.02.016>.
- 396 Cugerone, A., Cenki-Tok, B., Oliot, E., Muñoz, M., Barou, F., Motto-Ros, V., and Goff, E.L.,
397 2020, Redistribution of germanium during dynamic recrystallization of sphalerite: *Geology*,
398 v. 48, p. 236–241, <https://doi.org/10.1130/G46791.1>.
- 399 Di Benedetto, F., Bernardini, G.P., Costagliola, P., Plant, D., and Vaughan, D.J., 2005,
400 Compositional zoning in sphalerite crystals: *The American Mineralogist*, v. 90, p. 1384–
401 1392, <https://doi.org/10.2138/am.2005.1754>.
- 402 **[[Not cited in text.]]** Du, G., Zhuang, X., Querol, X., Izquierdo, M., Alastuey, A., Moreno, T.,
403 and Font, O., 2009, Ge distribution in the Wulantuga high-germanium coal deposit in the
404 Shengli coalfield, Inner Mongolia, northeastern China: *International Journal of Coal*
405 *Geology*, v. 78, p. 16–26, <https://doi.org/10.1016/j.coal.2008.10.004>.

- 406 Fougereuse, D., Cugerone, A., Reddy, S.M., Luo, K., and Motto-Ros, V., 2023, Nanoscale
407 distribution of Ge in Cu-rich sphalerite: *Geochimica et Cosmochimica Acta*, v. 346, p. 223–
408 230, <https://doi.org/10.1016/j.gca.2023.02.011>.
- 409 Fowler, A.D., and L'Heureux, I., 1996, Self-organized banded sphalerite and branching galena in
410 the Pine Point ore deposit, Northwest Territories: *Canadian Mineralogist*, v. 34, p. 1211–
411 1222.
- 412 Franchini, M., McFarlane, C., Maydagán, L., Reich, M., Lentz, D.R., Meinert, L., and Bouhier,
413 V., 2015, Trace metals in pyrite and marcasite from the Agua Rica porphyry–high
414 sulfidation epithermal deposit, Catamarca, Argentina: Textural features and metal zoning at
415 the porphyry to epithermal transition: *Ore Geology Reviews*, v. 66, p. 366–387,
416 <https://doi.org/10.1016/j.oregeorev.2014.10.022>.
- 417 Frenzel, M., Ketris, M.P., and Gutzmer, J., 2014, On the geological availability of germanium:
418 *Mineralium Deposita*, v. 49, p. 471–486, <https://doi.org/10.1007/s00126-013-0506-z>.
- 419 **[[Not cited in text.]]** Frenzel, M., Hirsch, T., and Gutzmer, J., 2016, Gallium, germanium,
420 indium, and other trace and minor elements in sphalerite as a function of deposit type—A
421 meta-analysis: *Ore Geology Reviews*, v. 76, p. 52–78,
422 <https://doi.org/10.1016/j.oregeorev.2015.12.017>.
- 423 Frenzel, M., Mikolajczak, C., Reuter, M.A., and Gutzmer, J., 2017, Quantifying the relative
424 availability of high-tech by-product metals—The cases of gallium, germanium and indium:
425 *Resources Policy*, v. 52, p. 327–335, <https://doi.org/10.1016/j.resourpol.2017.04.008>.
- 426 George, L.L., Cook, N.J., and Ciobanu, C.L., 2016, Partitioning of trace elements in co-
427 crystallized sphalerite-galena-chalcopyrite hydrothermal ores: *Ore Geology Reviews*, v. 77,
428 p. 97–116, <https://doi.org/10.1016/j.oregeorev.2016.02.009>.
- 429 Guizhou Bureau of Geology and Mineral Resources (GBGMR), 1987, *Regional Geology of*
430 *Guizhou Province*: Beijing, Geological Publishing House, 631 p.
- 431 Gulley, A.L., Nassar, N.T., and Xun, S., 2018, China, the United States, and competition for
432 resources that enable emerging technologies: *Proceedings of the National Academy of*
433 *Sciences of the United States of America*, v. 115, p. 4111–4115,
434 <https://doi.org/10.1073/pnas.1717152115>.
- 435 Höll, R., Kling, M., and Schroll, E., 2007, Metallogenesis of germanium—A review: *Ore*
436 *Geology Reviews*, v. 30, p. 145–180, <https://doi.org/10.1016/j.oregeorev.2005.07.034>.
- 437 **[[Not cited in text.]]** Hu, R.-Z., Qi, H.-W., Zhou, M.-F., Su, W.-C., Bi, X.-W., Peng, J.-T., and
438 Zhong, H., 2009, Geological and geochemical constraints on the origin of the giant Lincang
439 coal seam–hosted germanium deposit, Yunnan, SW China: A review: *Ore Geology*
440 *Reviews*, v. 36, p. 221–234, <https://doi.org/10.1016/j.oregeorev.2009.02.007>.
- 441 Johan, Z., 1988, Indium and germanium in the structure of sphalerite: An example of coupled
442 substitution with copper: *Mineralogy and Petrology*, v. 39, p. 211–229,
443 <https://doi.org/10.1007/BF01163036>.
- 444 **[[Not cited in text.]]** Keith, M., Haase, K.M., Schwarz-Schampera, U., Klemm, R., Petersen, S.,
445 and Bach, W., 2014, Effects of temperature, sulfur, and oxygen fugacity on the composition

- 446 of sphalerite from submarine hydrothermal vents: *Geology*, v. 42, p. 699–702,
447 <https://doi.org/10.1130/G35655.1>.
- 448 Kelley, K.D., Huston, D.L., and Peter, J.M., 2021, Toward an effective global green economy:
449 The Critical Minerals Mapping Initiative(CMMI): *SGA News*, v. 48, p. 1–6.
- 450 Lan, Z., Li, X., Zhu, M., Chen, Z.-Q., Zhang, Q., Li, Q., Lu, D., Liu, Y., and Tang, G., 2014, A
451 rapid and synchronous initiation of the widespread Cryogenian glaciations: *Precambrian*
452 *Research*, v. 255, p. 401–411, <https://doi.org/10.1016/j.precamres.2014.10.015>.
- 453 Lan, Z., Li, X.-H., Zhu, M., Zhang, Q., and Li, Q.-L., 2015, Revisiting the Liantuo Formation in
454 Yangtze block, South China: SIMS U-Pb zircon age constraints and regional and global
455 significance: *Precambrian Research*, v. 263, p. 123–141,
456 <https://doi.org/10.1016/j.precamres.2015.03.012>.
- 457 Lanari, P., Vidal, O., De Andrade, V., Dubacq, B., Lewin, E., Grosch, E.G., and Schwartz, S.,
458 2014, XMapTools: A MATLAB©-based program for electron microprobe X-ray image
459 processing and geothermobarometry: *Computers & Geosciences*, v. 62, p. 227–240,
460 <https://doi.org/10.1016/j.cageo.2013.08.010>.
- 461 Li, H., Zhou, Z.-K., Algeo, T.J., Wu, J.-H., and Jiang, W.-C., 2019, Geochronology and
462 geochemistry of tuffaceous rocks from the Banxi Group: Implications for Neoproterozoic
463 tectonic evolution of the southeastern Yangtze block, South China: *Journal of Asian Earth*
464 *Sciences*, v. 177, p. 152–176, <https://doi.org/10.1016/j.jseaes.2019.03.022>.
- 465 Liang, Q.-L., Xie, Z., Song, X.-Y., Wirth, R., Xia, Y., and Cline, J., 2021, Evolution of invisible
466 Au in arsenian pyrite in Carlin-type Au deposits: *Economic Geology*, v. 116, p. 515–526,
467 <https://doi.org/10.5382/econgeo.4781>.
- 468 Liu, W., Mei, Y., Etschmann, B., Glenn, M., MacRae, C.M., Spinks, S.C., Ryan, C.G., Brugger,
469 J., and Paterson, D.J., 2023, Germanium speciation in experimental and natural sphalerite:
470 Implications for critical metal enrichment in hydrothermal Zn-Pb ores: *Geochimica et*
471 *Cosmochimica Acta*, v. 342, p. 198–214, <https://doi.org/10.1016/j.gca.2022.11.031>.
- 472 Luo, K., Cugerone, A., Zhou, M.-F., Zhou, J.-X., Sun, G.-T., Xu, J., He, K.-J., and Lu, M.-D.,
473 2022, Germanium enrichment in sphalerite with acicular and euhedral textures: An example
474 from the Zhulingou carbonate-hosted Zn(-Ge) deposit, South China: *Mineralium Deposita*,
475 v. 57, p. 1343–1365, <https://doi.org/10.1007/s00126-022-01112-4>.
- 476 Paradis, S., 2015, Indium, germanium and gallium in volcanic- and sediment-hosted base-metal
477 sulphide deposits, in **Simandl, G.J., and Neetz, M., eds.**, *Symposium on Critical and*
478 *Strategic Materials Proceedings: British Columbia Ministry of Energy and Mines* **Special**
479 **Publication 2015-3**, p. 23–29.
- 480 Paton, C., Hellstrom, J., Paul, B., Woodhead, J., and Hergt, J., 2011, Iolite: Freeware for the
481 visualisation and processing of mass spectrometric data: *Journal of Analytical Atomic*
482 *Spectrometry*, v. 26, p. 2508–2518, <https://doi.org/10.1039/c1ja10172b>.
- 483 Phelps, P.R., Lee, C.-T.A., and Morton, D.M., 2020, Episodes of fast crystal growth in
484 pegmatites: *Nature Communications*, v. 11, 4986, [https://doi.org/10.1038/s41467-020-](https://doi.org/10.1038/s41467-020-18806-w)
485 [18806-w](https://doi.org/10.1038/s41467-020-18806-w).

- 486 **[Not cited in text.]** Qi, H.-W., Rouxel, O., Hu, R.-Z., Bi, X.-W., and Wen, H.-J., 2011,
 487 Germanium isotopic systematics in Ge-rich coal from the Lincang Ge deposit, Yunnan,
 488 southwestern China: *Chemical Geology*, v. 286, p. 252–265,
 489 <https://doi.org/10.1016/j.chemgeo.2011.05.011>.
- 490 Raimondo, T., Payne, J., Wade, B., Lanari, P., Clark, C., and Hand, M., 2017, Trace element
 491 mapping by LA-ICP-MS: Assessing geochemical mobility in garnet: *Contributions to*
 492 *Mineralogy and Petrology*, v. 172, p. 17, <https://doi.org/10.1007/s00410-017-1339-z>.
- 493 **[Not cited in text.]** Scott, S.D., 1973, Experimental calibration of the sphalerite geobarometer:
 494 *Economic Geology*, v. 68, p. 466–474, <https://doi.org/10.2113/gsecongeo.68.4.466>.
- 495 **[Not cited in text.]** Seredin, V.V., Danilcheva, Yu.A., Magazina, L.O., and Sharova, I.G., 2006,
 496 Ge-bearing coals of the Luzanovka graben, Pavlovka brown coal deposit, southern
 497 Primorye: *Lithology and Mineral Resources*, v. 41, p. 280–301,
 498 <https://doi.org/10.1134/S0024490206030072>.
- 499 Sun, G., Zeng, Q., Zhou, J.-X., Zhou, L., and Chen, P., 2021, Genesis of the Xinling vein-type
 500 Ag-Pb-Zn deposit, Liaodong Peninsula, China: Evidence from texture, composition and in
 501 situ S-Pb isotopes: *Ore Geology Reviews*, v. 133,
 502 <https://doi.org/10.1016/j.oregeorev.2021.104120>.
- 503 Tao, Y., Hu, R.Z., Tang, Y.Y., Ye, L., Qi, H.W., and Fan, H.F., 2019, Types of dispersed
 504 elements bearing ore deposits and their enrichment regularity in southwest China: *Acta*
 505 *Geologica Sinica*, v. 93, p. 1210–1230 [in Chinese with English abstract].
- 506 Torró, L., Millán-Nuñez, A.J., Benites, D., González-Jiménez, J.M., Laurent, O., Tavazzani, L.,
 507 Vallance, J., Chelle-Michou, C., Proenza, J.A., Flores, C., Melgarejo, J.C., Rosas, S., and
 508 Fontboté, L., 2023, Germanium- and gallium-rich sphalerite in Mississippi Valley-type
 509 deposits: The San Vicente district and the Shalipayco deposit, Peru: *Mineralium Deposita*,
 510 v. 58, p. 853–880, <https://doi.org/10.1007/s00126-023-01160-4>.
- 511 U.S. Geological Survey, 1996, *Mineral Commodity Summaries 1996*: Reston, Virginia, U.S.
 512 Geological Survey, 67 p.
- 513 U.S. Geological Survey, 2022, *Mineral Commodity Summaries 2022*: Reston, Virginia, U.S.
 514 Geological Survey, 71 p.
- 515 Wang, D.H., 2019, Study on critical mineral resources: Significance of research, determination
 516 of types, attributes of resources, progress of prospecting, problems of utilization and
 517 direction of exploitation: *Acta Geologica Sinica*, v. 93, p. 1189–1209 [in Chinese with
 518 English abstract].
- 519 Wang, L.-J., Griffin, W.L., Yu, J.-H., and O'Reilly, S.Y., 2010, Precambrian crustal evolution of
 520 the Yangtze block tracked by detrital zircons from Neoproterozoic sedimentary rocks:
 521 *Precambrian Research*, v. 177, p. 131–144, <https://doi.org/10.1016/j.precamres.2009.11.008>.
- 522 **[Not cited in text.]** Wei, C., Ye, L., Hu, Y., Danyushevskiy, L., Li, Z., and Huang, Z., 2019,
 523 Distribution and occurrence of Ge and related trace elements in sphalerite from the Lehong
 524 carbonate-hosted Zn-Pb deposit, northeastern Yunnan, China: Insights from SEM and LA-
 525 ICP-MS studies: *Ore Geology Reviews*, v. 115,
 526 <https://doi.org/10.1016/j.oregeorev.2019.103175>.

- 527 Wilson, S.A., Ridley, W.I., and Koenig, A.E., 2002, Development of sulfide calibration
 528 standards for the laser ablation inductively-coupled plasma mass spectrometry technique:
 529 Journal of Analytical Atomic Spectrometry, v. 17, p. 406–409,
 530 <https://doi.org/10.1039/B108787H>.
- 531 Wu, Y.-F., Fougereuse, D., Evans, K., Reddy, S.M., Saxey, D.W., Guagliardo, P., and Li, J.-W.,
 532 2019, Gold, arsenic, and copper zoning in pyrite: A record of fluid chemistry and growth
 533 kinetics: Geology, v. 47, p. 641–644, <https://doi.org/10.1130/G46114.1>.
- 534 Xian, H., Zhang, S., Li, H., Yang, T., and Wu, H., 2020, Geochronological and palaeomagnetic
 535 investigation of the Madiyi Formation, lower Banxi Group, South China: Implications for
 536 Rodinia reconstruction: Precambrian Research, v. 336,
 537 <https://doi.org/10.1016/j.precamres.2019.105494>.
- 538 Yao, W.-H., and Li, Z.-X., 2016, Tectonostratigraphic history of the Ediacaran–Silurian Nanhua
 539 foreland basin in South China: Tectonophysics, v. 674, p. 31–51,
 540 <https://doi.org/10.1016/j.tecto.2016.02.012>.
- 541 Ye, L., Cook, N.J., Ciobanu, C.L., Yuping, L., Qian, Z., Tiegeng, L., Wei, G., Yulong, Y., and
 542 Danyushevskiy, L., 2011, Trace and minor elements in sphalerite from base metal deposits
 543 in South China: A LA-ICPMS study: Ore Geology Reviews, v. 39, p. 188–217,
 544 <https://doi.org/10.1016/j.oregeorev.2011.03.001>.
- 545 **[[Not cited in text.]]**Zartman, R.E., and Doe, B.R., 1981, Plumbotectonics—The model:
 546 Tectonophysics, v. 75, p. 135–162, [https://doi.org/10.1016/0040-1951\(81\)90213-4](https://doi.org/10.1016/0040-1951(81)90213-4).
- 547 Zhai, M.G., Wu, F.Y., Hu, R.Z., Jiang, S.Y., Li, W.C., Wang, R.C., Wang, D.H., Qi, T., Qin,
 548 K.Z., and Wen, H.J., 2019, Critical metal mineral resources: Current research status and
 549 scientific issues: Bulletin of National Natural Science Foundation of China, v. 33, p. 106–
 550 111 [in Chinese with English abstract].
- 551 Zhou, L., McKenna, C.A., Long, D.G.F., and Kamber, B.S., 2017, LA-ICP-MS elemental
 552 mapping of pyrite: An application to the Palaeoproterozoic atmosphere: Precambrian
 553 Research, v. 297, p. 33–55, <https://doi.org/10.1016/j.precamres.2017.05.008>.
- 554 Zhou, L., Fan, H., and Ulrich, T., 2021a, Editorial for Special Issue “Critical Metals in
 555 Hydrothermal Ores: Resources, Recovery, and Challenges”: Minerals (Basel), v. 11,
 556 <https://doi.org/10.3390/min11030299>.
- 557 Zhou, J.-X., Yang, D.Z., Yu, J., Luo, K., and Zhou, Z.H., 2021b, The discovery of Ge
 558 enrichment in the Zhulingou Zn deposits in Guiding, Guizhou Province: Geology in China,
 559 v. 48, p. 665–666 [in Chinese].

560

561 Figure 1. Binary plot showing the Zn-Ge resources of major Ge-rich base metal deposits
 562 worldwide. Dashed lines indicate the Ge contents of sphalerite. Abbreviation: AGR—
 563 Aangouran, Iran; BBJ—Banbianjie, China; DLZ—Daliangzi, China; EG—Elmwood-
 564 Gordonsville, Tennessee, USA; FK—Fankou, China; FL—Fule, China; HZ—Huize, China;
 565 JD—Jinding, China; KP—Kipushi, Namibia; LS—Lisheen, Ireland; MP—Maoping, China;
 566 MY—Mayuan, China; NV—Naven, Ireland; NYZ—Nayongzhi, China; QS—Qingshan, China;
 567 RD—Red Dog, Alaska, USA; SM—Silvermines, Ireland; SS—Saint-Salvy, France; TBS—


568 Tianbaoshan, China; TM—Tsumeb, Namibia; WSH—Wusihe, China; ZLG—Zhulingou, China.
 569 **[[Figure edit: Define SEDEX in caption.]]**

570 Figure 2. (A) **Structural** map of the southeastern margin of the Yangtze block, South China. Red
 571 rectangle represents the study area. (B) Geological map of the SE Yangtze block with the
 572 location of the Banbianjie deposit. **[[Figure edit: Add N and E to lat and long designations.]]**

573 Figure 3. (A) Geological map of the Banbianjie deposit. (B) Cross section of No. 1 exploration
 574 line. (C) General stratigraphy of the Banbianjie area. **[[Figure edits: Add N and E to lat and
 575 long designations. American English spelling of gray throughout C.]]**

576 Figure 4. Field photographs of the Zn-Ge mineralization in the Banbianjie deposit. (A)
 577 Stratabound sulfide with local veins crosscutting dolostone bedding (white dotted lines). Red
 578 dotted lines highlight the sulfide veins crosscutting bedding. (B) Stratabound sulfide veins
 579 parallel to bedding. (C) Stratabound sulfide veins with few dolostone brecciated clasts with
 580 rounded shapes. The breccia is cemented by a sulfide mass. (D) Colloform sphalerite, pyrite, and
 581 marcasite bands. Dolomite filled the empty space. (E) Sp₂ veinlets filling fractures in dolostone.
 582 (F) Lumpy aggregates of Sp₂ with a significant presence of organic matter. (G) Sp₂-calcite
 583 veins. Abbreviations: Cal—calcite; Mas—marcasite; Py—pyrite; Sp₁—sphalerite 1; Sp₂—
 584 sphalerite 2.


585 Figure 5. Representative photomicrographs showing textures of type 1 ore. (A) Disseminated
 586 sphalerite (Sp_{1a}) and pyrite (Py_{1a}) in host rocks, followed by colloform sphalerite (Sp_{1b}) and
 587 pyrite (Py_{1b}) assemblages. (B) Oscillatory zoned Sp_{1b} in transmitted plane-polarized light. Dark
 588 Sp_{1b} is acicular, whereas the light Sp_{1b} is mostly euhedral. (C) Euhedral Py_{1b} intergrown with
 589 acicular marcasite. (D) Deformed Sp_{1b} with intense microfractures. (E) Colloform Sp_{1b}
 590 overgrown by Py_{1b}, followed by calcite and euhedral barite. (F) Oscillatory zoned Sp_{1b} with
 591 darker color and acicular texture in the core, and lighter color and euhedral texture on the rim.
 592 Abbreviations: Brt—barite; Cal—calcite; Mas—marcasite; Py_{1a}—pyrite 1a; Py_{1b}—pyrite 1b;
 593 Sp_{1a}—sphalerite 1a; Sp_{1b}—sphalerite 1b.

594 Figure 6. Representative photomicrographs showing the texture of type 2 ore. (A) Sp₂-dolomite
 595 vein and brecciated fragments of type 1 ore (reflected light). Sp_{1b} and Sp_{1b}-Py_{1b} brecciated
 596 clasts have an angular shape. (B) Sp₂-dolomite veins and brecciated fragments of Sp_{1b}
 597 (transmitted light). Type 1 ore clasts are cemented by dolomite. (C) Oscillatory zoning of Sp₂
 598 with the location of the laser ablation–inductively coupled plasma–mass spectrometry (LA-ICP-
 599 MS) trace-element data points. (D) Brecciated fragments of Sp_{1b} cemented by dolomite. (E)
 600 Colloform Sp₂ along fractures with minor Py₂ and Mas₂. Abbreviations: Dol—dolomite; Gn—
 601 galena; Mas₂—marcasite 2; Py₂—pyrite 2; Sp_{1b}—sphalerite 1b; Sp₂—sphalerite **type 2**.
 602 **[[Figure edit: Capitalize Fig. 9E label in C.]]** 

603 Figure 7. Paragenetic sequence of the Banbianjie deposit. Abbreviations: Sp_{1a}—sphalerite 1a;
 604 Sp_{1b}—sphalerite 1b; Sp₂—sphalerite 2.

605 Figure 8. Box plot showing selected trace-element variations of Sp1a, Sp1b, and Sp2.
 606 Abbreviations: Sp1a—sphalerite 1a; Sp1b—sphalerite 1b; Sp2—sphalerite 2. **[[Figure edit: Add**
 607 **vertical-axis label and put units in parentheses: Concentration (ppm).]]**

608 Figure 9. Laser ablation–inductively coupled plasma–mass spectrometry (LA-ICP-MS) element
 609 maps of **colloform sphalerite (Sp1b) and pyrite (Py1b)**.


610 Figure 10. Laser ablation–inductively coupled plasma–mass spectrometry (LA-ICP-MS)
 611 elemental maps of Sp2 **[[Define type here?]]**. Abbreviations: Sp2—sphalerite 2. 


612 Figure 11. Transect showing trace-element variations in Sp1b and Sp2 from the Banbianjie
 613 deposit. (A–B) Location of laser ablation–inductively coupled plasma–mass spectrometry (LA-
 614 ICP-MS) points in Sp1b. (C–D) Trace-element variations in Sp1b from the profile in A–B. (E)
 615 Trace-element variations in Sp2 (location of this profile is shown in Fig. 6C). Abbreviations:
 616 Mas—marcasite; Py1a—pyrite 1a; Py1b—pyrite 1b; Sp1a—sphalerite 1a; Sp1b—sphalerite 1b
 617 Sp2—sphalerite 2. **[[Figure edit: Add vertical-axis label and put units in parentheses in C–**
 618 **E: Trace element (ppm).]]**

619 Figure 12. Transmission electron microscopy (TEM) images of Ge-rich nanoparticles in Sp1b.
 620 (A) High-angle annular dark-field (HAADF) image showing two Ge-rich nanoparticles (NP) in
 621 Sp1b. (B) Detailed HAADF image showing a rounded Ge-rich NP. Elongated structure is
 622 interpreted as a fracture. (C) HAADF image showing three Ge-rich nanoparticles in Sp1b. (D)
 623 Close-up of image in C, showing that the nanoparticle is lighter than Sp1b in the HAADF image.
 624 (E) Close-up of image in D, showing that the Ge-rich nanoparticle seems to be an assemblage.
 625 (F) High-resolution transmission electron microscopy (HRTEM) image showing the planes of
 626 Ge-rich nanoparticle and Sp1b. Abbreviations: NP—nanoscale particles; Sp1b—sphalerite 1b.

627 Figure 13. Binary plots for trace-element contents in sphalerite from the Banbianjie deposit. (A)
 628 Ge vs. Fe. (B) Ge vs. Cd. (C) Mn vs. Ge. (D) Cu vs. Ge. (E) Pb vs. Ge. (F) Ga vs. Cd.
 629 Abbreviations: Sp1a—sphalerite 1a; Sp1b—sphalerite 1b; Sp2—sphalerite 2

630 Figure 14. (A) Binary plot for Pb vs. Ge. (B) Ge/Pb ratios for different types of sphalerite and
 631 Zn-Ge-Pb-S nanoparticles. Abbreviations: Sp1a—sphalerite 1a; Sp1b—sphalerite 1b; Sp2—
 632 sphalerite 2; NP—nanoscale particles.

633 Figure 15. Comparison of Cd, Ge, and Pb contents ($\mu\text{mol/g}$) in sphalerite. (A) Ternary diagram
 634 showing three compositional groups (Grp). Grp1 with high Pb contents represents pyrite.
 635 Because we used $^{66}\text{Zn} = 650,000$ ppm as an internal standard, pyrite has overestimated Pb
 636 contents relative to sphalerite. Grp 2 has higher Ge and Pb and lower Cd contents than Grp3. (B)
 637 Pixel identification map with the three groups discriminated in A. (C) Laser ablation–inductively
 638 coupled plasma–mass spectrometry (LA-ICP-MS) data ($\mu\text{mol/g}$) values across the line A–B 
 639 indicated in B. (D) Ternary diagram showing three groups. Grp1, with high Pb contents,
 640 represents galena and dolomite. Grp 2 has higher Ge and Pb and lower Cd contents than Grp3.
 641 Larger Ge contents in Sp2 are noted compared to Sp1b. (E) Pixel identification map with the

642 three groups discriminated in D. (F) LA-ICP-MS data ($\mu\text{mol/g}$) values across the line ~~C-D~~ 
643 indicated in E. Abbreviations: Py1b—pyrite 1b; Sp1b—sphalerite 1b; Sp2—sphalerite 2.
644 **[[Figure edits: Define Nam in caption. Add axis labels to plots in C and F: Content**
645 **($\mu\text{mol/g}$).]]]]**

646 Figure 16. Schematic model of Ge enrichment in sphalerite from the Banbianjie deposit. On the
647 right, the diagrams **illustrate** the relative changes in Zn-Ge-Pb and Cd-Ga concentrations, in the
648 abundance of nanoparticles (NPs), and in the sphalerite (Sp) growth rate. (A) In stage 1, acicular
649 and euhedral grains of Sp1b show oscillatory zoning. (B) In stage 2, acicular crystals of Sp2
650 exhibit only oscillatory zoning. Brecciated clasts of Sp1 can be seen on the right of this sketch.
651 Abbreviations: Py—pyrite; Sp1b—sphalerite 1b; Sp1a—sphalerite 1a; Sp2—sphalerite 2.